AGU100 ADVANCING EARTH AND SPACE SCIENCE

Geophysical Research Letters

RESEARCH LETTER
10.1029/2020GL087629

Special Section:
The Ice, Cloud and land Elevation Satellite-2 (ICESat-2) on-orbit performance, data discoveries and early science

Observing Waves in Sea Ice With ICESat-2

C. Horvat[1], Ed Blanchard-Wrigglesworth[2], and A. Petty[3,4]

[1]Institute at Brown for Environment and Society, Brown University, Providence, RI, USA, [2]Department of Atmospheric Science, University of Washington, Seattle, WA, USA, [3]Earth System Science Interdisciplinary Center, University of Maryland, College Park, MD, USA, [4]NASA Goddard Space Flight Center, Greenbelt, MD, USA

Abstract The coupled interaction of ocean surface waves and sea ice is important in determining the thermodynamic and dynamic properties of sea ice and its relationship to the ocean and atmosphere. Wave-ice interactions create the marginal ice zone (MIZ), a region critically important for ecology, transportation, and the polar energy budget. Typically, the MIZ is defined using satellite products as those regions where sea ice concentration is between 15% and 80%. Here we present a new technique to observe ocean surface waves in sea ice, leveraging NASA's ICESat-2 satellite laser altimeter, and produce maps of wave-affected sea ice regions in both hemispheres. Defining a new wave-based metric for MIZ extent, we find that compared to a concentration-based metric, wave-based MIZ estimates are smaller. Further, the wave-affected MIZ makes up a larger fraction of sea ice extent in winter than in summer, opposite to the seasonal cycle of concentration-based MIZ.

Key Points:
- Ocean surface waves propagating through sea ice can be observed in IceSat-2 altimetry
- Filtering for areas of wave-ice activity, we create global maps of wave-affected sea ice regions and the marginal ice zone
- Marginal ice zone extent differs in magnitude and seasonal cycle when defined by wave activity versus sea ice concentration

Supporting Information:
- Supporting Information S1

Correspondence to:
C. Horvat,
horvat@brown.edu

Citation:
Horvat, C., Blanchard-Wrigglesworth, E., & Petty, A. A. (2020). Observing waves in sea ice with ICESat-2. *Geophysical Research Letters*, *47*, e2020GL087629. https://doi.org/10.1029/2020GL087629

Received 24 FEB 2020
Accepted 22 APR 2020
Accepted article online 23 APR 2020

1. Introduction

Ocean waves, whether locally generated wind waves or long-period swell waves, are increasingly observed in the Arctic (Thomson & Rogers, 2014) and are a persistent feature of Southern Ocean sea ice (Squire et al., 1995). In the presence of ocean waves, sea ice floes bend, and if the wave field is sufficiently energetic, will break—impacting the sea ice floe size distribution (FSD) without significantly changing sea ice concentration or thickness (Langhorne et al., 1998). Fractured sea ice is mobile and susceptible to lateral melting—thus, a feedback between ocean surface waves, the FSD, and floe melting has been hypothesized (e.g., Asplin et al., 2012; Horvat et al., 2016; Kohout & Meylan, 2008), with potential impacts for sea ice predictability.

The marginal ice zone (MIZ) is defined as the region "where waves and swells affect the ice" (NSIDC, 2019), or more broadly the "part of the ice cover which is close enough to the open ocean boundary to be affected by its presence" (Wadhams, 2013). It is where coupled interactions between sea ice fragmentation, air-sea exchange, and ocean surface waves are most dynamic. Absent methods for detecting wave-ice interactions at global scales over long time periods, the MIZ has traditionally been defined by identifying regions of concentration between 15% and 80% using passive microwave satellite observations (Comiso et al., 1997; Strong & Rigor, 2013; Strong et al., 2017). Ice charts, drawn combining satellite data and visual obserations, can be different to PM-SIC observations (Agnew & Howell, 2003), though have not been used to produce basin-scale MIZ statistics. It has been suggested that the Arctic MIZ is expanding (Aksenov et al., 2017; Thomson & Rogers, 2014) although it may simply be moving poleward, taking up a larger fraction of retreating sea-ice-covered regions (Rolph et al., 2019). Less focus has been paid to the larger (defined based on concentration) Antarctic MIZ (Stroeve et al., 2016).

Concentration-based definitions of the MIZ can deviate from dynamically based ones. In winter months, waves propagating through high-concentration ice might not alter overall sea ice concentration because leads refreeze and would not be classified as MIZ. Winter months have the highest seasonal storminess and associated wave activity at both poles and therefore the effects of strong wave activity, like sea ice growth processes (Lange et al., 1989) or ocean turbulence (Li et al., 2016) may be largest. In summer months, regions of low sea ice concentration can form through surface or basal melting far from contact with ocean surface waves, leading to sea ice uninfluenced by the open ocean classified as MIZ. Basin-wide observations of waves in sea ice are needed at high temporal resolution to improve understanding of the MIZ and address questions of its changing character at both poles.

Efforts underway to simulate fully coupled interactions between waves and sea ice in climate models (Boutin et al., 2018; Bateson et al., 2020; Horvat & Tziperman, 2015; Roach et al., 2018, 2019; Williams et al., 2013) involve uncertainty about modeling waves in sea ice (Meylan & Squire, 1994; Shen, 2019; Squire, 2007, 2018; Voermans et al., 2019; Wang & Shen, 2010). There is a lack of observations covering the wide range of potential ocean and ice states to refine and compare them (Collins et al., 2015). Emergent metrics like MIZ extent and direct measurements of waves in ice will prove useful constraints.

Here we present new altimetric estimates of ocean waves in sea ice using the ICESat-2 (IS-2) laser altimeter. Ocean waves have long been studied with the use of satellite altimeters (e.g., Jackson et al., 1985; Stopa et al., 2016; Sun et al., 2005), which provide near-real-time, one-dimensional measurements of the ocean surface with high frequency and high along-track resolution. The promise of using (radar) altimetry to observe waves in the sea ice and the MIZ was first presented by (Rapley, 1984), but related efforts have been limited, as waveform models designed for the open ocean are not applicable over sea ice, where wave energies are weaker, and are expressed through the sea ice, with its own heterogeneous and anisotropic surface field. Satellite-based Synthetic Aperture Radar (SAR) imagery has been used to resolve swell and high-frequency wind wave spectra in ice (Ardhuin et al., 2017, 2019; Stopa et al., 2018), though with low measurement frequencies (e.g., less than 60 scenes per year for $2° \times 4°$ regions in the Southern Ocean; supporting information Stopa et al., 2018) because of challenges in automatic detection and separation of waves and ice features (Stopa et al., 2018). Initial data generated by IS-2 have shown promise for profiling waves in the open ocean, due to its combination of high sampling rate and vertical accuracy together with its small footprint (Klotz et al., 2020). Direct detection of vertical variations of the ice surface could indicate the presence of waves within the ice pack.

2. ICESat-2 Altimetry Data

The sole instrument on-board ICESat-2 is the photon-counting Advanced Topographic Laser Altimeter System (ATLAS); a low pulse-energy laser with 1.5 ns pulse width and high pulse repetition rate (10 kHz, 70 cm pulse spacings) split into a six-beam configuration of three strong/weak beam pairs. We utilize the L3A along-track sea ice height and type product (ATL07 Kwok et al., 2019) derived primarily from the Level 2A ATL03 photon heights (Neumann et al., 2019). Segment heights $\{h\}$ are generated by aggregating 150 photons (from ATL03) along each beam, resulting in segments of variable length $\{l\}$ (see the ATBD for more details, Kwok et al., 2019). Mean segment lengths in ATL07 for strong beams are approximately 17 m, for mean segment resolutions of approximately 31 mx 14 m (combined with the ~14 m laser footprint) (Kwok et al., 2019). Ocean surface waves have O(100 m) wavelengths and propagate at O(1) m/s, thus along-track measurements are likely unaffected by wave dynamics over the ATL07 sampling window. An empirical decision tree determines whether a given segment is ice or water (*height_segment_type*). IS-2 surface heights are adjusted based on reference geoidal and tidal variations and inverted barometer effects (Kwok et al., 2019).

ATL07 data are only provided where passive microwave data indicate a sea ice concentration above 15%. Surface waves can bias height retrievals, and the effect of this bias in the open ocean is still being explored with ICESat-2 (Klotz et al., 2020; Morison et al., 2019). Our aim is to detect the presence of wave activity within the ice pack rather than detailed wave profiling/sea state bias estimates, for which a more comprehensive assessment of ATL07 (and ATL03) is likely needed.

3. Observing Waves in Sea Ice With IceSat-2: A Case Study in the Barents Sea

To show clear evidence that IS-2 can detect waves in sea ice we begin by studying a case study of a swell event in the Barents sea. Figure 1a plots the trajectory of a descending (southward) IS-2 profile of the Barents Sea region at 17:00 GMT on 22 March 2019, the significant wave height (SWH, the average height of the 1/3 highest waves Michel, 1968) on 3/22 from NOAA's Wavewatch III production hindcast (WW3), and the 15% and 85% ice concentration contours from the NASA Team passive microwave product (herafter PM-SIC) (Cavalieri et al., 1996)—to verify the presence of ice we also compared to the SMOS sea ice thickness product (Huntemann et al., 2014) with similar results. On 3/22 a large cyclonic system drifted toward the Barents and interacted with a developing low pressure system north of Svalbard, producing high surface westerly winds of approximately 60–100 km/hr over the Norwegian Sea. This storm resulted in eastward-propagating surface waves with SWHs of up to 10 m. An ascending IS-2 profile over the region 12 hr later intersected a

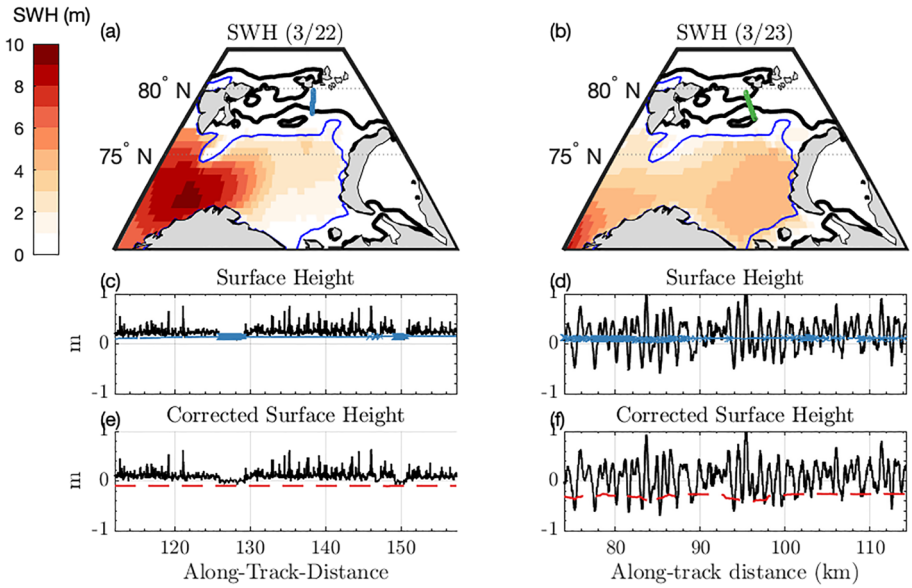

Figure 1. Identifying waves in ice before and after a storm from IS-2 ATL07 surface height data. (a) Significant wave height (colors) from WW3 on 22 March 2019 in the Barents Sea. Blue/black contours are 15% and 85% PM-SIC contours. Thick blue line is part of IS-2 track at 16:00 GMT. (b) Same as (a) but 12 hr later on 23 March 2019, with IS-2 track at 04:00 GMT in green. (c) ATL07 surface height fields for the 22 March track. Sea surface points scattered as blue crosses on the 50 km SSH field η. (e) Corrected surface height field $h - \eta$. Red dashed line is $-\nu$, where ν is the greater of 10 cm, or the 10-km standard deviation of sea surface height or ice surface height. (d and f) Same as (c) and (e), for the 23 March track. (c), (e), (d), and (f) cover the same latitude range.

nearby, similarly ice-covered region (green line, Figure 1b). By this time the low-pressure system had moved east over Novya Zemlya, with the ocean swell traveling into the Barents Sea, where SWH was 4 m.

Figures 1c and 1d show the surface height field taken for segments identified as sea ice for both tracks, using beam 2L for both the descending track on 22 March and the ascending track on 23 March. Before the storm swell encountered the sea-ice region in (a), surface heights were positive (Figure 1c). After the storm swell reached this region, the surface height profile changes dramatically (Figure 1d). The small-amplitude vertical variations on 22 March are replaced by large (up to 1 m in amplitude), wave-like variations in surface height. Despite the increased variability of the sea ice height field, the average surface height of ice points over this latitude range differs by just 1 cm between the two dates, suggesting that the observed surface height variability on 23 March reflects the presence of waves in ice.

3.1. Identifying Waves, Wave Energetics, and Wave Statistics in ATL07

Deviations in the sea surface caused by oceanic or atmospheric circulation can lead to a negative (or positive) bias in the ice surface height that is not the result of wave activity. We first isolate all ATL07 segments identified as ocean surface points (*height_segment_type* > 1)—leads would be classified as ocean surface, but sea ice points would not. We then linearly interpolate a sea surface height field to each segment location using the estimated sea surface segment heights (*height_segment_height*). Because waves present in the sea ice will also be manifest in the ocean, we use a 50 km moving average to arrive at a mesoscale anomaly sea level field η, the local 50 km average deviation from the reference sea surface height, a field related to dynamic ocean topography (Armitage et al., 2017; Morison et al., 2012). This surface height field is plotted as blue solid lines in Figures 1c and 1d, with ocean surface points scattered along it as blue hashes. We provide maps of η in the Arctic and Southern Ocean as Figures S1 and S2, and this field is included as a part of the supporting data.

In this first effort to obtain bulk wave-ice statistics from altimetric data, we will identify areas in which waves are present using a series of thresholding criteria. This methodology is captured in Figures 1e and 1f, where we plot the rescaled surface height field, $h - \eta$. Although there is a minor qualitative alteration of the surface height field as a result of bias correction, as before nearly all 22 March segments (Figure 1e) are positive with low-amplitude variability, and a significant fraction of 23 March (Figure 1f) tracks are negative with

high-amplitude oscillations. Note that in summer months, *height_segment_type* > 1 may also include areas of sea ice covered by melt ponds. Thus, we caution against overinterpreting this rescaling in those months.

In the supporting information, Text S1 and Figure S7, we use a nonuniform Fourier transform to examine the spectral characteristics of the signals in Figures 1e and 1f. This wave-like signal is clearly evident as a peak at a wavelength of approximately 1 km for the 23 March data, with the spectral characteristics outside of that band similar between the two tracks. Thus, we do not believe this signal is the product of some other ice or ocean-related physical phenomenon. The along-track measurements are at an unknown angle to the direction of wave propagation, meaning this should be an overestimate of the actual wavelength of these waves. A 1 km surface gravity wave has a period of 25 s, substantially larger than the peak period of approximately 15 s recorded in the Barents Sea by WW3 on 22 March. Thus, there is a bias that prevents the immediate retrieval of wave statistics like wave energy, significant wave height, or peak period from this data. Correcting for this bias will be the focus of future work comparing along-track Fourier analysis to in situ data (see Section 5 and Text S1).

Our desire is to identify a set of criteria by which we judge individual segments to be "wave-affected." We first filter appropriate ice segments as those that are less than 200 m long and that have at least two positive (ssh adjusted) along-track segment height measurements within 1 km. This eliminates fewer than 1% of all tracks, primarily anomalously long returns caused by low photon rates (i.e., low information density) and anomalous regions of consistently small but negative surface heights. For segments that pass these elementary filters, negative values of the rescaled surface height might indicate the presence of waves. However, uncertainty or variability in both the height of sea surface tie points and sea ice points can cause negative deviations in $h - \eta$ that are not the product of waves. We therefore define an along-track variable ν as the greater of the 10 km standard deviation of the interpolated sea surface height field, the 10 km standard deviation of the surface height field, or 10 cm (red dashed lines, Figures 1e and 1f). Then we define a segment as wave affected if it meets three criteria (W1–W3):

W1: It has a sufficiently negative surface height ($h - \eta + \nu < 0$).

Using W1 restricts the definition of wave activity to those areas where the wave amplitudes are large relative to the adjusted ice surface height. Over the full IS-2 data set (see Section 4), the mean $h_i - \eta$ value is 34 cm, and the mean of ν is 20 cm. Our method is therefore restricted to only observing waves whose amplitude is appropriately large (i.e., for an "average" sea ice height and variance, an amplitude of 54 cm or larger), and we note that a bias may exist because the set of possible wave energies found using this threshold method decreases as sea ice surface heights increase.

W2: It has at least one sea surface tie point within a 10 km window centered at its location.

The criterion W2 ensures that areas where the sea surface height bias cannot be estimated are not considered wave affected. Points that fail to satisfy W2 can be found in pack ice regions of the Arctic (see Figure S1), where floes are extensive and compact and accurate estimates of the sea surface height bias difficult to make. We therefore assume these segments are *not* wave affected as they are far from areas of open water or leads. This is a conservative assumption, as waves can affect pack ice, particularly during storms. Yet it is not feasible to bias-correct the segment heights far from tie points as this can lead to anomalous regions of wave activity in areas of compact pack ice.

W3: There are at least two negative (ssh adjusted) along-track segment height measurements within a 1 km window centered at its location.

The final criterion W3 eliminates individual anomalous negative surface heights.

In the 22 March track, no segments meet W1–W3. In the 23 March track, 15% do. The percentage of segments by length that meet W1–W3 will always be less than the length of a region that might be considered "wave affected" as this threshold only identifies parts of the negative (trough) phase of a wave. When compiling a total length of fractures, we multiply by two (to include the positive [crest] of the wave) but address how this may be ameliorated in the supporting information (Text S3) by adjusting the observed lengths as a function of wave energy and ice surface height.

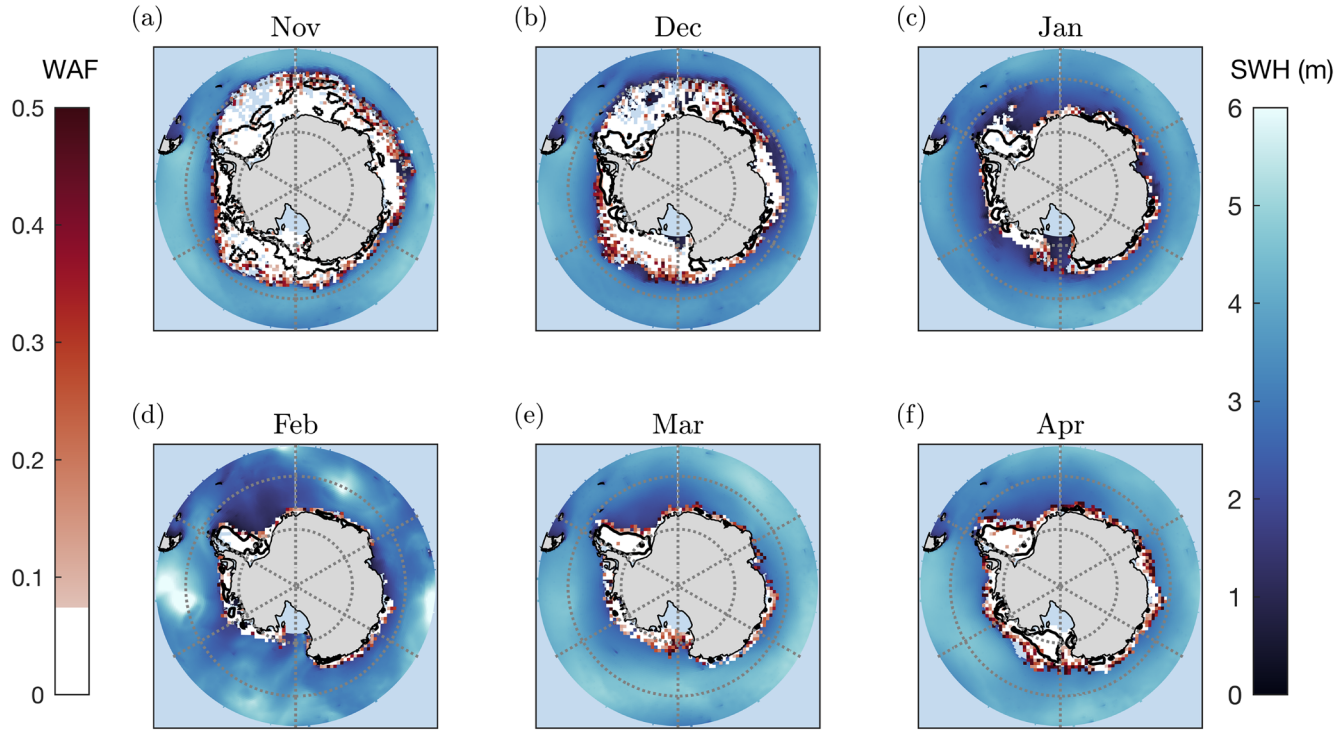

Figure 2. Wave-affected regions in the Southern Ocean. Wave affected fraction (WAF) in the Southern Ocean for (a) November 2018 to (f) April 2019. Colorbar cuts off regions where WAF is less than 7.5%. Black contour is 80% PM-SIC. Blue colors are monthly WW3 significant wave heights and correspond to right colorbar. April WW3 data are from 2018.

4. Global Statistics of Waves in Ice

To produce synoptic scale statistics of waves in ice (e.g., monthly maps of the MIZ), we process all beams across both hemispheres from 14 October 2018 to 31 August 2019, for a total of 4.5 billion individual segments. Each individual beam is preprocessed and bias-corrected as in Section 3.1. Segments are then binned into a 100 km × 100 km polar stereographic grid in each month in each hemisphere, and we define the total segment length (TSL) for a given grid cell,

$$\mathrm{TSL} = \sum_i l_i, \tag{1}$$

where i iterates over all segments. An individual segment is considered "wave affected" if it meets W1–W3, and we define the "wave affected length,"

$$\mathrm{WAL} = 2 \sum_j l_j, \tag{2}$$

where now j runs over all segments that meet W1–W3. We crudely multiply by two because our method can only identify the negative (trough) phase of a wave, which must have a positive (crest) phase. The "wave affected fraction" WAF is further defined:

$$\mathrm{WAF} = \frac{\mathrm{WAL}}{\mathrm{TSL}}. \tag{3}$$

The effect of this filtering on maps of WAF is given as Text S2 and Figure S3.

Figure 2 plots maps of WAF and monthly averaged SWH for the Southern Ocean for monthly periods from November 2018 to April 2019. The colorbar cuts off regions where WAF < 7.5%, a threshold chosen to segment out regions with low, potentially noise-induced "waviness" and include as many possible wave-affected regions as possible. In the supporting information, we reproduce Figures 2 and 3 without this threshold, showing that interior sea-ice-covered regions have small but nonzero values of WAF, which result from imperfect filtering (Figures S4 and S5) and justifying the choice of this threshold. Most wave activity is found

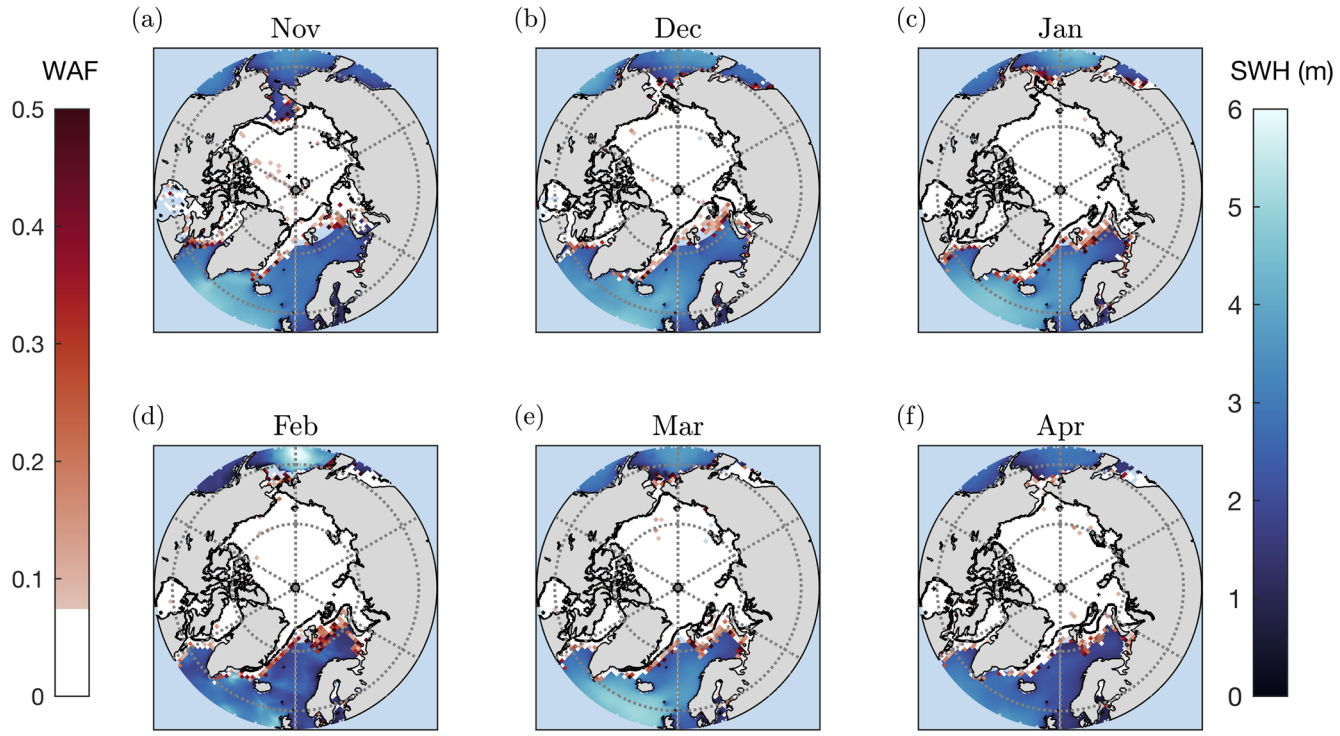

Figure 3. Wave-affected regions in the Arctic Ocean. Wave affected fraction (WAF) in the Arctic Ocean for (a) November 2018 to (f) April 2019. Colorbar cuts off regions where WAF is less than 7.5%. Black contour is 80% PM-SIC. Blue colors are monthly WW3 significant wave heights and correspond to right colorbar. April WW3 data are from 2018.

along the sea ice margin, though the width of those regions changes seasonally. From November–February the Weddell Sea and East Antarctic regions show lower WAF, consistent with lower SWH during that period. The location of the 80% sea ice concentration contour (black line) shows a spatial coherence between IS-2 wave-affected regions and PM-SIC-classified MIZ. Areas of low sea ice concentration, but not wave activity, are found more from November–December (a and b), with greater spatial consistency between low-concentration and wave-affected areas from January–April (c–f), especially in the Weddell Sea.

We reproduce Figure 2 in the Arctic Ocean as Figure 3. Much like in the Southern Ocean, we see the presence of wave activity in the form of a wide MIZ in the Bering Sea, Baffin Bay, Fram Strait, and Barents Sea, correlated with regions of higher average significant wave heights. Higher SWH from December–March compared to April in the Greenland and Barents Seas, for example, correspond to wider regions of wave-affected sea ice. The most consistent region of high wave-ice activity is the Barents Sea region. In the supporting information (Figures S8 and S9), we show zoomed-in plots of the Atlantic sector and Bering Sea in these months. The location of wave-affected regions is generally spatially consistent with areas of low-concentration sea ice (black contour), although found in a narrower band at the ice edge. As in the Southern Hemisphere (though in the opposite season), the MIZ width using PM-SIC is wider than using WAF in November–December but improves from January–April.

We next seek to produce global statistics of the MIZ width and its relation to total sea ice extent. The total number of segment retrievals in the Antarctic is plotted as a solid line in Figure 4a, corresponding to the left axis in units of millions. This is repeated for the Arctic in Figure 4b. Note that IS-2 data were compromised for much of July 2019 due to an observatory reorientation malfunction, leading to reduced segment counts. In Figures 4c–4f we interpolate from June–August and scatter values obtained from limited July tracks.

We start by defining a "sea ice extent" in each month using IS-2, adding the area of all 100 km × 100 km grid cell areas with at least 15,000 (in the Arctic) or 6,000 (in the Southern Ocean) individual segment measurements, plotted as blue solid lines in Figures 4c and 4d. These thresholds were chosen to produce similar seasonal cycles and spatial maps of sea ice extent as from passive microwave (dashed blue lines, and see Figures 2 and 3). The lower threshold in the Southern Ocean is because of the equatorward latitude of

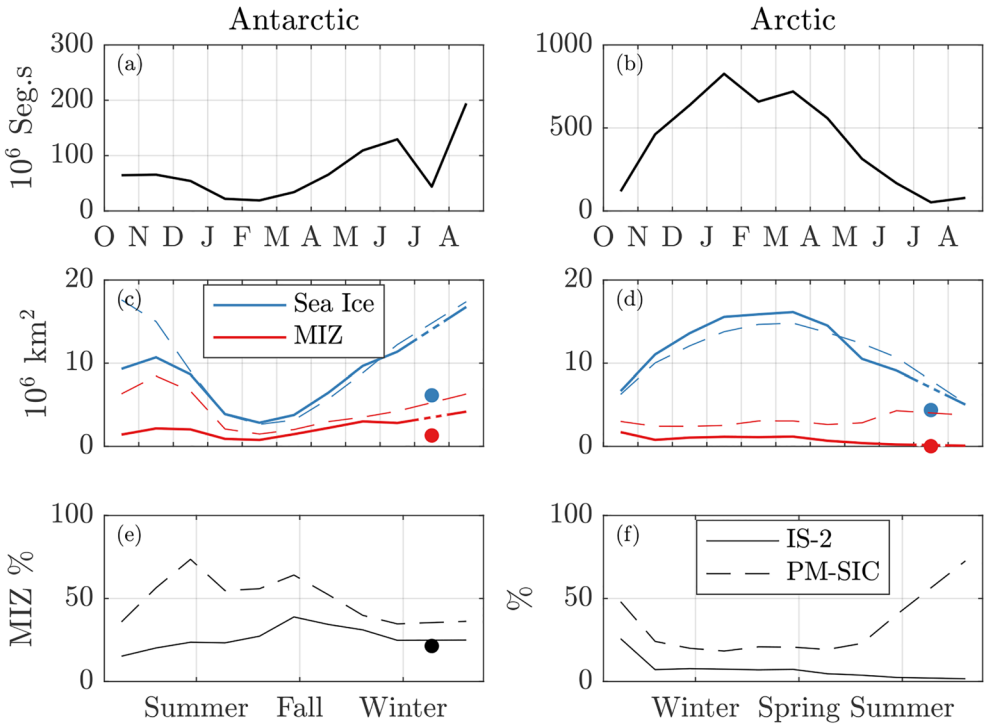

Figure 4. October 2018 to August 2019 marginal ice zone and sea ice extent. (a) Number of segment retrievals (divided by 1 million) for Antarctic sea ice (solid line, left axis) in each month. (c) Sea ice extent (solid blue) and marginal ice zone extent (solid red) from IS-2 in the Arctic from October 2018 to August 2019. Dashed lines are concentration-based from PM-SIC. (e) Fraction of sea ice extent that is marginal ice zone from IS-2 (solid) and PM-SIC (dashed). Filled circles are estimates from available data in July 2019. (b, d, and f) Same as (a), (c), and (e) for the Arctic.

ice-covered areas relative to Arctic sea ice points and therefore lower track density. Although IS-2 is not intended to produce statistics of sea ice extent, it reproduces the temporal and spatial seasonal cycle of sea ice extent over almost all months. An exception is October–November 2018 in the Southern Hemisphere, where segment densities are anomalously low: Comparing November 2018 and August 2019, PM-SIC extents are similar (15×10^6 km^3 in November vs. 17×10^6 km^3 in August), but segment counts are dramatically smaller (65 million in November vs. 194 million in August). While IS-2 was operational for only a fraction of October 2018, the reason for this discrepancy in November is unknown. It may be further investigated as the IS-2 data continue to become available. Overall, we have confidence that our method can be used to obtain seasonal variations in the type and extent of sea ice in polar regions.

We define the wave-affected MIZ extent as the integral over all areas with WAF > 7.5% (solid red lines) and compare this to the traditional concentration-based definition of MIZ extent (dashed red lines) in Figures 4c and 4d. In Figures 4e and 4f we plot the fraction of sea ice extent classified as MIZ from (solid line) IS-2 and (dashed line) PM-SIC. In both hemispheres, the MIZ fraction is larger when defined using PM-SIC. Antarctic IS-2 MIZ fraction rises from 24% in November to 40% in March–April before decreasing into winter. Arctic MIZ fraction is largest in winter and smallest in summer, opposite to PM-SIC MIZ fraction, and is less than 10% of total sea ice extent in all months save for October.

The seasonal variation of IS-2 and PM-SIC estimates of MIZ extent are generally consistent from fall to spring in both hemispheres (Figure 3), although MIZ extent magnitudes are substantially different in the Arctic. Both passive microwave estimates of sea ice concentration and IS-2 retrievals of wave activity are more uncertain in summer, and a comparison in both hemispheres during periods of high surface meltwater coverage may not be appropriate here due to potential corruption of the method when melt ponds are identified as sea surface tie points. In August, when less of Arctic sea ice may be ponded compared to June and July (Fetterer & Untersteiner, 1998), the estimate of MIZ extent from PM-SIC exceeds 50% of Arctic sea ice coverage, whereas less than 4% of IS-2-observed Arctic sea ice is classified as MIZ using the wave-based definition.

5. Discussion and Conclusion

Significant attention has been paid to how the MIZ has and will change using definitions based on ice concentration. Here we designed a method to observe waves in sea ice with the ICESat-2 altimeter and produce the first seasonal cycle of the MIZ using a definition based on the occurrence of waves in ice. Our results demonstrate a spatial coherence of wave-affected regions and low-concentration areas that is most significant in winter but may diverge in summer.

We suggest two reasons for the differences in MIZ extent comparing WAF to that from PM-SIC. First is the interpretation of altimetric returns. Recovering along-track surface height spectra could ameliorate this issue by disentangling sea ice from ocean surface variability (see Text S1 and Figure S6). We found this method applicable in individual case studies, but as the relative orientation in the satellite ground track and wave train is unknown, a systematic method for obtaining spectra from IS-2 tracks remains a challenge. Wave events have shorter persistence than sea ice concentration changes, and IS-2 may not capture all events, underestimating WAF. The penetration of low-amplitude waves into the ice pack may lead to low-concentration sea ice into the ice pack—explaining why despite the spatial consistency between the PM-SIC and WAF-based MIZs, there can be large differences in MIZ extent.

The second is that regions of low sea ice concentration are not necessarily regions of high wave activity. Low ice concentrations in summer pack ice, or far from the ice edge, do not imply small floes nor the presence of ocean surface waves and apart from being lower-concentration may have similar properties to pack ice. Examining local and regional variability in wave-affected and low-concentration sea ice, particularly in areas like the North Barents Sea, would help to elucidate the importance of waves.

This work is exploratory. We possess less than a single year of IS-2 measurements, and IS-2 algorithm development is still ongoing. We have not performed ground-truthing against buoys or SAR imagery, though new campaigns and measurement tools (e.g., Rabault et al., 2020) present an opportunity to make this comparison as that data become available. Our filtering techniques, while tying appropriately with concentration-based estimates of sea ice extent and MIZ extent in winter, and producing intuitive maps of Arctic and Southern Ocean wave and MIZ variability, have not been evaluated against other products. Extrapolating from the seasonal coupling-decoupling of waves and ice concentration is therefore not justified at this early stage. The MIZ is not uniquely defined, and other dynamically based definitions may be useful in different contexts. We hope to investigate the use of spectral methods to understand the propagation and attenuation of waves in sea ice and validate this methodology against other remote sensed and in situ products and other metrics of MIZ extent.

Despite challenges in adopting and verifying this new technique, IS-2 altimetry represents a unique opportunity to observe waves in sea ice and define the MIZ mechanistically. Coincident measurements, especially with SAR (Ardhuin et al., 2017; Stopa et al., 2018), wave buoy-based spectral measurements of waves in ice (Marchenko et al., 2019; Rabault et al., 2020; Smith & Thomson, 2016), and of the FSD (Horvat et al., 2019), will be necessary to refine and increase confidence in this methodology, increasing the number of observations of waves in ice by orders of magnitude.

Data Availability Statement

ICESat-2 data are available through the National Snow and Ice Data Center (NSIDC). The sea ice height product is found online (at https://nsidc.org/data/ATL07/versions/2). Beam-by-beam processed fields used in this study as. mat output files are provided as supporting data and will be made available as a PANGAEA data archive in compliance with FAIR Data Standards upon paper acceptance. Code that is used to process data will be available and updated on github upon paper acceptance (at https://github.com/chhorvat/ICESAT-Waves).

Acknowledgments
C. H. was supported by the NOAA Climate and Global Change Postdoctoral Fellowship Program, sponsored in part through Cooperative Agreement NA16NWS4620043, Years 2017–2021, with the National Oceanic and Atmospheric Administration, U.S. Department of Commerce. E. B. W. was supported by NASA Grant NNX17AI33G.

References

Agnew, T., & Howell, S. (2003). The use of operational ice charts for evaluating passive microwave ice concentration data. *Atmosphere-Ocean*, *41*(4), 317–331. https://doi.org/10.3137/ao.410405

Aksenov, Y., Popova, E. E., Yool, A., Nurser, A. J., Williams, T. D., Bertino, L., & Bergh, J. (2017). On the future navigability of Arctic sea routes: High-resolution projections of the Arctic Ocean and sea ice. *Marine Policy*, *75*, 300–317. https://doi.org/10.1016/j.marpol.2015.12.027

Ardhuin, F., Stopa, J. E., Chapron, B., Collard, F., Husson, R., Jensen, R. E., & Young, I. (2019). Observing sea states. *Frontiers in Marine Science*, *6*(APR), 1–29. https://doi.org/10.3389/fmars.2019.00124

Ardhuin, F., Stopa, J., Chapron, B., Collard, F., Smith, M., Thomson, J., & Wadhams, P. (2017). Measuring ocean waves in sea ice using SAR imagery: A quasi-deterministic approach evaluated with Sentinel-1 and in situ data. *Remote Sensing of Environment*, *189*, 211–222. https://doi.org/10.1016/j.rse.2016.11.024

Armitage, T. W. K., Bacon, S., Ridout, A. L., Petty, A. A., Wolbach, S., & Tsamados, M. (2017). Arctic Ocean surface geostrophic circulation 2003-2014. *The Cryosphere*, *11*(4), 1767–1780. https://doi.org/10.5194/tc-11-1767-2017

Asplin, M. G., Galley, R., Barber, D. G., & Prinsenberg, S. (2012). Fracture of summer perennial sea ice by ocean swell as a result of Arctic storms. *Journal of Geophysical Research*, *117*, 1–12. https://doi.org/10.1029/2011JC007221

Bateson, A. W., Feltham, D. L., Schröder, D., Hosekova, L., Ridley, J. K., & Aksenov, Y. (2020). Impact of sea ice floe size distribution on seasonal fragmentation and melt of Arctic sea ice. *The Cryosphere*, *14*(2), 403–428. https://doi.org/10.5194/tc-14-403-2020

Boutin, G., Ardhuin, F., Dumont, D., Sévigny, C., Girard-Ardhuin, F., & Accensi, M. (2018). Floe size effect on wave-ice interactions: Possible effects, implementation in wave model, and evaluation. *Journal of Geophysical Research: Oceans*, *123*, 4779–4805. https://doi.org/10.1029/2017JC013622

Cavalieri, D. J., Parkinson, C. L., Gloerson, P., & Zwally, H. J. (1996). Sea ice concentrations from Nimbus-7 SMMR and DMSP SSM/I-SSMIS passive microwave data. NASA National Snow and Ice Data Center Distributed Active Archive Center, https://doi.org/10.5067/8GQ8LZQVL0VL

Collins, C. O., Rogers, W. E., Marchenko, A., & Babanin, A. V. (2015). In situ measurements of an energetic wave event in the Arctic marginal ice zone. *Geophysical Research Letters*, *42*, 1863–1870. https://doi.org/10.1002/2015GL063063

Comiso, J. C., Cavalieri, D. J., Parkinson, C. L., & Gloersen, P. (1997). Passive microwave algorithms for sea ice concentration: A comparison of two techniques. *Remote Sensing of Environment*, *60*(3), 357–384. https://doi.org/10.1016/S0034-4257(96)00220-9

Fetterer, F., & Untersteiner, N. (1998). Observations of melt ponds on Arctic sea ice. *Journal of Geophysical Research*, *103*(C11), 24,821–24,835. https://doi.org/10.1029/98JC02034

Horvat, C., Roach, L. A., Tilling, R., Bitz, C. M., Fox-Kemper, B., Guider, C., & Shepherd, A. (2019). Estimating the sea ice floe size distribution using satellite altimetry: Theory, climatology, and model comparison. *The Cryosphere*, *13*(11), 2869–2885. https://doi.org/10.5194/tc-13-2869-2019

Horvat, C., & Tziperman, E. (2015). A prognostic model of the sea-ice floe size and thickness distribution. *Cryosphere*, *9*(6), 2119–2134. https://doi.org/10.5194/tc-9-2119-2015

Horvat, C., Tziperman, E., & Campin, J. M. (2016). Interaction of sea ice floe size, ocean eddies, and sea ice melting. *Geophysical Research Letters*, *43*, 8083–8090. https://doi.org/10.1002/2016GL069742

Huntemann, M., Heygster, G., Kaleschke, L., Krumpen, T., Mäkynen, M., & Drusch, M. (2014). Empirical sea ice thickness retrieval during the freeze-up period from SMOS high incident angle observations. *Cryosphere*, *8*, 439–451. https://doi.org/10.5194/tc-8-439-2014

Jackson, F. C., Walton, W. T., & Baker, P. L. (1985). Aircraft and satellite measurement of ocean wave directional spectra using scanning-beam microwave radars. *Journal of Geophysical Research*, *90*(C1), 987. https://doi.org/10.1029/JC090iC01p00987

Klotz, B. W., Neuenschwander, A., & Magruder, L. A. (2020). High-resolution ocean wave and wind characteristics determined by the ICESat-2 land surface algorithm. *Geophysical Research Letters*, *47*, 1–10. https://doi.org/10.1029/2019GL085907

Kohout, A. L., & Meylan, M. H. (2008). An elastic plate model for wave attenuation and ice floe breaking in the marginal ice zone. *Journal of Geophysical Research*, *113*, C09016. https://doi.org/10.1029/2007JC004434

Kwok, R., Cunningham, G., Hancock, D., Ivanoff, A., & Wimert, J. (2019). *Ice, Cloud, and Land Elevation Satellite-2 Project: Algorithm Theoretical Basis Document (ATBD) for sea ice products*. Pasadena, CA, USA: NASA Goddard Space Flight Center.

Kwok, R., Cunningham, G., Markus, T., Hancock, D., Morison, J., Palm, S. P., & Team, t. I. S. (2019). ATLAS/ICESat-2 L3A sea ice height, Version 1. Boulder, Colorado USA. May, Boulder, Colorado USA, NSIDC, https://doi.org/10.5067/ATLAS/ATL07.001

Kwok, R., Markus, T., Kurtz, N. T., Petty, A. A., Neumann, T. A., Farrell, S. L., & Wimert, J. T. (2019). Surface height and sea ice freeboard of the Arctic Ocean from ICESat-2: Characteristics and early results. *Journal of Geophysical Research: Oceans*, *124*, 6942–6959. https://doi.org/10.1029/2019JC015486

Lange, M., Ackley, S., Wadhams, P., Dieckmann, G., & Eicken, H. (1989). Development of sea ice in the Weddell Sea. *Annals of Glaciology*, *12*, 92–96. https://doi.org/10.3189/S0260305500007023

Langhorne, P. J., Squire, V. A., Fox, C., & Haskell, T. G. (1998). Break-up of sea ice by ocean waves. *Annals of Glaciology*, *27*, 438–442. https://doi.org/10.3189/S0260305500017869

Li, Q., Webb, A., Fox-Kemper, B., Craig, A., Danabasoglu, G., Large, W. G., & Vertenstein, M. (2016). Langmuir mixing effects on global climate: WAVEWATCH III in CESM. *Ocean Modelling*, *103*, 145–160. https://doi.org/10.1016/j.ocemod.2015.07.020

Marchenko, A., Wadhams, P., Collins, C., Rabault, J., & Chumakov, M. (2019). Wave-ice interaction in the North-West Barents Sea. *Applied Ocean Research*, *90*, 101,861. https://doi.org/10.1016/j.apor.2019.101861

Meylan, M. H., & Squire, V. A. (1994). The response of ice floes to ocean waves. *Journal of Geophysical Research*, *99*(C1), 891. https://doi.org/10.1029/93JC02695

Michel, W. H. (1968). Sea spectra simplified. *Mar Technology*, *5*(1), 17–30.

Morison, J., Hancock, D., Dickinson, S., Robbins, J., Roberts, L., Kwok, R., & Team, I. S. (2019). Ice, Cloud, and Land Elevation Satellite-2 Project: Algorithm Theoretical Basis Document (ATBD) for ocean surface height. Seattle, WA, USA, NASA Goddard Space Flight Center, https://icesat-2.gsfc.nasa.gov/sites/default/files/page_files/ICESat2_ATL12_ATBD_r001.pdf

Morison, J., Kwok, R., Peralta-Ferriz, C., Alkire, M., Rigor, I., Andersen, R., & Steele, M. (2012). Changing Arctic Ocean freshwater pathways. *Nature*, *481*(7379), 66–70. https://doi.org/10.1038/nature10705

NSIDC (2019). Cryosphere Glossary: The Marginal Ice Zone. nsidc.org/cryosphere/glossary/term/marginal-ice-zone

Neumann, T. A., Martino, A. J., Markus, T., Bae, S., Bock, M. R., Brenner, A. C., & Thomas, T. C. (2019). The Ice, Cloud, and Land Elevation Satellite 2 mission: A global geolocated photon product derived from the Advanced Topographic Laser Altimeter System. *Remote Sensing of Environment*, *233*, 111,325. https://doi.org/10.1016/j.rse.2019.111325

Rabault, J., Sutherland, G., Gundersen, O., Jensen, A., Marchenko, A., & Breivik, Ø. (2020). An open source, versatile, affordable waves in ice instrument for scientific measurements in the Polar Regions. *Cold Regions Science and Technology*, *170*, 102955. https://doi.org/10.1016/j.coldregions.2019.102955

Rapley, C. G. (1984). First observations of the interaction of ocean swell with sea ice using satellite radar altimeter data. *Nature*, *307*(5947), 150–152. https://doi.org/10.1038/307150a0

Roach, L. A., Bitz, C. M., Horvat, C., & Dean, S. M. (2019). Advances in modeling interactions between sea ice and ocean surface waves. *Journal of Advances in Modeling Earth Systems*, *11*, 4167–4181. https://doi.org/10.1029/2019MS001836

Roach, L. A., Smith, M. M., & Dean, S. M. (2018). Quantifying growth of pancake sea ice floes using images from drifting buoys. *Journal of Geophysical Research: Oceans*, *123*, 2851–2866. https://doi.org/10.1002/2017JC013693

Rolph, R. J., Feltham, D. L., & Schröder, D. (2019). Changes of the Arctic marginal ice zone. *The Cryosphere Discuss*, *November*, 1–18. https://doi.org/10.5194/tc-2019-224

Shen, H. H. (2019). Modelling ocean waves in ice-covered seas. *Applied Ocean Research*, *83*, 30–36. https://doi.org/10.1016/J.APOR.2018.12.009

Smith, M., & Thomson, J. (2016). Scaling observations of surface waves in the Beaufort Sea. *Elementa: Science of the Anthropocene*, *4*(1), 000097. https://doi.org/10.12952/journal.elementa.000097

Squire, V. A. (2007). Of ocean waves and sea-ice revisited. *Cold Regions Science and Technology*, *49*(2), 110–133. https://doi.org/10.1016/j.coldregions.2007.04.007

Squire, V. A. (2018). A fresh look at how ocean waves and sea ice interact. *Philosophical Transactions of the Royal Society A: Mathematical, Physical and Engineering Sciences*, *376*(2129), 20170342. https://doi.org/10.1098/rsta.2017.0342

Squire, V. A., Dugan, J. P., Wadhams, P., Rottier, P. J., & Liu, A. K. (1995). Of ocean waves and sea ice. *Annual Review of Fluid Mechanics*, *27*(1), 115–168. https://doi.org/10.1146/annurev.fl.27.010195.000555

Stopa, J. E., Ardhuin, F., & Girard-Ardhuin, F. (2016). Wave climate in the Arctic 1992–2014: Seasonality and trends. *The Cryosphere*, *10*(4), 1605–1629. https://doi.org/10.5194/tc-10-1605-2016

Stopa, J. E., Ardhuin, F., Thomson, J., Smith, M. M., Kohout, A., Doble, M., & Wadhams, P. (2018). Wave attenuation through an arctic marginal ice Zone on 12 October 2015: 1. Measurement of wave spectra and ice features from Sentinel 1A. *Journal of Geophysical Research: Oceans*, *123*, 3619–3643. https://doi.org/10.1029/2018JC013791

Stopa, J. E., Sutherland, P., & Ardhuin, F. (2018). Strong and highly variable push of ocean waves on Southern Ocean sea ice. *Proceedings of the National Academy of Sciences*, *115*(23), 5861–5865. https://doi.org/10.1073/pnas.1802011115

Stroeve, J. C., Jenouvrier, S., Campbell, G. G., Barbraud, C., & Delord, K. (2016). Mapping and assessing variability in the Antarctic marginal ice zone, pack ice and coastal polynyas in two sea ice algorithms with implications on breeding success of snow petrels. *The Cryosphere*, *10*(4), 1823–1843. https://doi.org/10.5194/tc-10-1823-2016

Strong, C., Foster, D., Cherkaev, E., Eisenman, I., & Golden, K. M. (2017). On the definition of marginal ice zone width. *Journal of Atmospheric and Oceanic Technology*, *34*(7), 1565–1584. https://doi.org/10.1175/JTECH-D-16-0171.1

Strong, C., & Rigor, I. G. (2013). Arctic marginal ice zone trending wider in summer and narrower in winter. *Geophysical Research Letters*, *40*(18), 4864–4868. https://doi.org/10.1002/grl.50928

Sun, J., Burns, S. P., Vandemark, D., Donelan, M. A., Mahrt, L., Crawford, T. L., & French, J. R. (2005). Measurement of directional wave spectra using aircraft laser altimeters. *Journal of Atmospheric and Oceanic Technology*, *22*(7), 869–885. https://doi.org/10.1175/JTECH1729.1

Thomson, J., & Rogers, W. E. (2014). Swell and sea in the emerging Arctic Ocean. *Geophysical Research Letters*, *41*, 3136–3140. https://doi.org/10.1002/2014GL059983

Voermans, J. J., Babanin, A. V., Thomson, J., Smith, M. M., & Shen, H. H. (2019). Wave attenuation by sea ice turbulence. *Geophysical Research Letters*, *46*, 6796–6803. https://doi.org/10.1029/2019GL082945

Wadhams, P. (2013). The seasonal ice zone. In N. Untersteiner (Ed.), *The Geophysics of Sea Ice* (pp. 825–830). Boston, MA: Springer.

Wang, R., & Shen, H. H. (2010). Gravity waves propagating into an ice-covered ocean: A viscoelastic model. *Journal of Geophysical Research*, *115*, C06024. https://doi.org/10.1029/2009JC005591

Williams, T. D., Bennetts, L. G., Squire, V. A., Dumont, D., & Bertino, L. (2013). Wave-ice interactions in the marginal ice zone. Part 1: Theoretical foundations. *Ocean Modelling*, *71*, 81–91. https://doi.org/10.1016/j.ocemod.2013.05.010